International Journal of Aeronautical and Space Sciences
https://doi.org/10.1007/s42405-019-00165-6

IJASS International Journal of Aeronautical and Space Sciences

ORIGINAL PAPER

The Effects of Wing Mass Asymmetry on Low-Speed Flight Characteristics of an Insect Model

Anh Tuan Nguyen[1] · Jae-Hung Han[2] · Thanh Trung Vu[1,3]

Received: 16 May 2018 / Revised: 11 March 2019 / Accepted: 3 April 2019

Abstract

Wing asymmetries can be found in real insects and flapping-wing micro air vehicles. This paper investigates some characteristics, including the trim conditions, power requirements and passive open-loop dynamics of an insect model with the asymmetry in wing mass in low-speed flight. The motion of the insect model is obtained through a simulation framework that couples an unsteady vortex-lattice method and a multibody dynamics code. The results show that a heavier wing has to be moved with a larger stroke amplitude to compensate for the wing mass asymmetry. The power required by the heavier wing is also found greater. Moreover, we can observe the asymmetries in lateral dynamics while comparing dynamic responses due to rightward and leftward gust disturbances.

Keywords Insect flight · Insect unsteady aerodynamics · Unsteady vortex-lattice method

List of Symbols

a_1	Squire's parameter
$\mathbf{B}$	Control effectiveness matrix
$\bar{c}$	Mean wing chord
D	Drag
F	Force
f	Flapping frequency
$\mathbf{G}$	Set of applied forces and gyroscopic terms of the inertia force
I	Moment of inertia
L	Lift
l_1	Distance from the body center to the wing-base pivot
M	Moment
m	Mass
$\boldsymbol{n}$	Normal vector
$\mathbf{P}$	Matrix used to project the applied forces
P	Power
p	Pressure
$\mathbf{Q}$	Mass matrix
$\mathbf{q}$	Set of coordinates representing displacements
R	Wing length
r_2	Second moment of the wing area
r_c	Vortex core radius
t	Time
$\boldsymbol{V}$	Velocity vector of flow
v	Velocity of the insect
x, y, z	Coordinates
α	Rotation angle
α_L	Lamb constant
β	Stroke plane angle
Γ	Circulation
$\boldsymbol{\gamma}$	Surface vorticity
$\boldsymbol{\eta}$	Set of applied motion constraints
η_s	Coefficient of leading-edge suction efficiency
θ	Elevation angle
Λ	Sweep angle
ρ	Air density
τ	Torque
υ	Kinematic viscosity
ϕ	Sweep angle
χ	Body angle

Electronic supplementary material The online version of this article (https://doi.org/10.1007/s42405-019-00165-6) contains supplementary material, which is available to authorized users.

✉ Jae-Hung Han
jaehunghan@kaist.ac.kr

[1] Faculty of Aerospace Engineering, Le Quy Don Technical University, Ha Noi, Vietnam

[2] Department of Aerospace Engineering, KAIST, Daejeon 34141, Republic of Korea

[3] Office of International Cooperation, Le Quy Don Technical University, Ha Noi, Vietnam

Published online: 04 May 2019

Subscripts

0	Mean value
amp	Amplitude
b	Body-fixed
bd	Body
G	Ground-fixed
L.E.	Leading-edge
ref	Reference
sp	Stroke plane
wg	Wing

Superscripts

a	Aerodynamics
as	Asymmetric
i	Inertial
l	Left wing
lg	Leftward gust
s	Symmetric
r	Right wing
rg	Rightward gust

1 Introduction

Recently, we have witnessed a rapidly increasing number of studies on various aspects of insect flight, including unsteady aerodynamics, flexible wing structures, as well as flight dynamics and control. The knowledge from these studies could be very useful for the designs of insect-like flapping-wing micro air vehicles (FWMAVs) [1–5]. Future insect-like FWMAVs are expected to possess the outstanding characteristics of insect flight in the wild, such as the ability to hover and undertake many types of sudden maneuvers with only a pair of wings [6, 7].

So far, most of studies regarding insect flight have dealt with the perfect condition of wing symmetries. It means in these studies, left and right wings were assumed to be exactly the same in terms of mass and geometry. However, in reality, wing asymmetries may exist due to many reasons, and one of these is the difference in wing mass. According to a statistical analysis of O'Hara and Palazotto on 30 hawkmoth individuals [8], the average difference in mass between left and right wings is about 3%. For some individuals, this difference may go up to 17%, which is believed to have a huge impact on their flight performance. For insect-like FWMAVs, the difference in wing mass can occur due to the imperfections of the manufacturing process.

Several researchers have empirically studied some types of asymmetric conditions in insect flight, such as Fernandez et al. [9] and Muijres et al. [10] for asymmetric wing damages, and Kassner et al. [11] for a wing loss condition. It should be noted that during these empirical studies, some physical details of insect flight dynamics may not be determined precisely. For example, experiments on living insects cannot show the passive open-loop dynamics of insect flight. In this work, for the first time, the numerical multibody dynamics approach is used to predict the effect of the wing mass asymmetry on several important flight characteristics of a hawkmoth *Manduca sexta* model at a low speed. For low-speed flight, the effect of the body aerodynamics can be neglected for the sake of simplicity [12]. In fact, the asymmetry in wing mass may occur along with the difference in area between left and right wings. However, to gain better insight into the effect of wing mass asymmetry, this difference is ignored in the present work, and the two wings are assumed to have the same wing planforms and dimensions. The right wing is assumed 10% heavier, and its moment of inertia is correspondingly 10% larger than that of the left wing. A multibody dynamics code is coupled with an aerodynamic model based the unsteady vortex-lattice method (UVLM) [12, 13] to simulate the free flight dynamics. The trim search algorithm [13, 14] is applied to obtain the equilibrium flight states. Through the derived asymmetric trim conditions, the differences in wing kinematics, downward flow velocity and power consumption between the left and right wings are indicated. Additionally, passive open-loop responses due to constant leftward and rightward lateral gust disturbances of the same magnitude are computed and compared with each other in an effort to show the asymmetric flight dynamics of the current insect model.

2 Materials and Methods

2.1 Insect Model and Wing Kinematics

The insect model used in this paper (Fig. 1) has the wing shape and mass properties of the hawkmoth *Manduca sexta* [8, 15]. The two wings have the same planform and dimensions; however, the mass and moment of inertia of the right wing are assumed 10% larger than those of the left wing. Some main

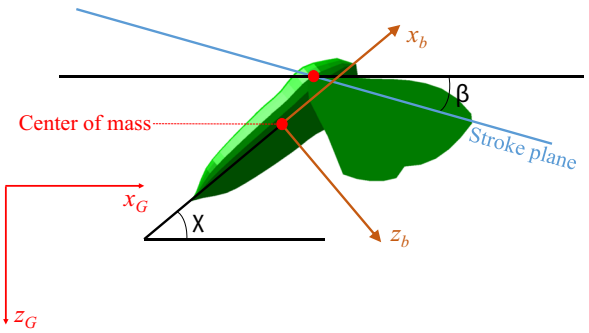

Fig. 1 Insect model and coordinate systems

parameters, including the mass of the right and left wings (m^{r}_{wg} and m^{l}_{wg}), wing length R, mean chord length $\bar{c}$, radius of the second moment of the wing area r_2, body mass m_{bd}, body length L_{bd}, distance from the body center to the wing-base pivot l_1 are given in Table 1.

The ground-fixed ($x_G y_G z_G$) and body-fixed ($x_b y_b z_b$) coordinate systems, which are shown in Fig. 1, will be used for the simulations in this work. The ground-fixed coordinate system has a vertically downward axis z_G and a forward x_G axis. The x_b axis of the body-fixed coordinate system coincides with the body axis of the insect model. A stroke plane angle β is defined as an angle between the stroke plane and the horizontal plane. A body angle χ is formed by the body axis and its projection onto the horizontal plane.

Each wing is connected to the body by a three degree-of-freedom (3-DOF) revolute joint, and the wing orientation relative to the stroke plane is determined by a rotation sequence of three Euler angles (i.e., the sweep angle ϕ, the elevation angle θ, and the rotation angle α). According to Nguyen et al. [12], the insect model changes the sweep angle ϕ to move its wings back and forth, whereas the elevation angle θ is used to move the wings upward and downward. α denotes the rotation angle of the wings about their feathering axes. More details about the definitions of these angles are given in Ref. [12]. The three Euler angles ϕ, θ and α are given in the form of third-order Fourier series:

$$[\phi(t)\ \theta(t)\ \alpha(t)] = \frac{a_0}{2} + \sum_{k=1}^{3} (a_k \cos(k2\pi ft) + b_k \sin(k2\pi ft)), \tag{1}$$

where f is the flapping frequency, and a_k and b_k are Fourier coefficients, whose values are determined based on measurement data [16].

2.2 Aerodynamic Model

In this paper, we study the asymmetry effect of a hawkmoth model flying at 1 m/s, which is typical for low-speed flight [12]. Nguyen et al. [13] proved that when the flight speed of the hawkmoth *Manduca sexta* is below 4 m/s, the effects of body aerodynamics on the flight characteristics are small. Therefore, for the sake of simplicity, it is possible to ignore the contribution of the body aerodynamics. To compute aerodynamic loads, the unsteady vortex-lattice method (UVLM), which has been used by Senda et al. [17, 18], Roccia et al. [19], and Nguyen et al. [12, 13, 20], is employed. According to this, the wings are represented by a system of quadrilateral or triangular vortex rings. Based on the result of the convergence study conducted by Nguyen et al. [12], the use of 72 vortex ring panels for each wing (Fig. 2) and 100 time steps per cycle is sufficient to obtain the converged aerodynamic force. Each vortex ring panel has a collocation point located at the panel's center. The no-penetration boundary condition is applied at the collocation points to assure that the velocity of the flow relative to the wing is parallel to the wing surface. The Kutta condition is applied at the trailing edges of the wings to allow all vortices along these edges to be shed entirely into the surrounding flow and form a free wake. The wake geometry is deformed and updated every computational time step. The wake nodes transport freely with the local velocity of the flow field. Herein, induced velocities are determined by the Bio–Savart law, and the pressure difference Δp between the lower and upper surfaces is computed by the unsteady Bernoulli equation:

$$\Delta p = \rho\left[\left(\boldsymbol{V}_{rel} \times \boldsymbol{\gamma}\right) \cdot \boldsymbol{n} + \frac{\partial \Gamma}{\partial t}\right], \tag{2}$$

where ρ is the fluid density, $\boldsymbol{V}_{rel}$ is the relative velocity of the flow to the wing surface, $\boldsymbol{\gamma}$ is surface vorticity, $\boldsymbol{n}$ is the normal vector of the wing surface, and Γ is the circulation of the local vortex ring.

The current UVLM is extended using the leading-edge suction analogy to compute the vortex force, and the vortex-core growth model to account for viscous diffusion [12]. According to an observation by Ellington et al. [21], the leading-edge vortex on an insect wing has a conical, spiral form similar to that on a delta wing. Thus, the leading-edge vortex force of an insect wing can be computed by the leading-edge suction analogy model that has been used for delta wings [22]. The magnitude of the leading-edge vortex force is [12]

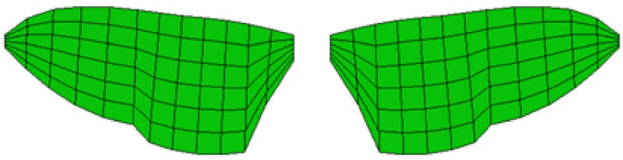

Fig. 2 Vortex ring panels

Table 1 Mass and morphological parameters of the insect mode

Parameter	m^{r}_{wg} (mg)	m^{l}_{wg} (mg)	R (mm)	$\bar{c}$ (mm)	S (mm^2)	r_2 (–)	m_{bd} (mg)	L_{bd} (mm)	l_1/L_{bd} (–)
Value	44.53	49.22	48.50	16.81	815.33	0.53	1485.0	44.80	0.25

$$F_{\mathrm{v}} = \frac{\pi}{16} \frac{\eta_{\mathrm{s}} \rho \Gamma_{\mathrm{L.E.}}^2}{\Delta x_{\mathrm{L.E.}} \cos \Lambda_{\mathrm{L.E.}}}, \tag{3}$$

where η_{s} denotes the coefficient of leading-edge suction efficiency, which is equal to 0.5 for hawkmoth wing aerodynamics [12]; $\Gamma_{\mathrm{L.E.}}$, $\Delta x_{\mathrm{L.E.}}$, and $\Lambda_{\mathrm{L.E.}}$ are the circulation, the length, and the sweep angle of the local leading-edge panel, respectively. It should be noted that when the local angle of attack at the leading edge exceeds a limit value, the leading-edge vortex force F_{v} is perpendicular to the wing surface. Otherwise, the flow is assumed attached and this force remains parallel to the local wing chord. Similar to the literature [12], the limit value of the angle of attack is 12°.

As mentioned above, the vortex-core growth model is applied to the wake to include the effect of viscous diffusion. The core radius r_{c} of each vortex line in the wake increases as time progresses [23]:

$$r_{\mathrm{c}}(t) = \sqrt{4\alpha_{\mathrm{L}} \nu \left(1 + a_1 \frac{\Gamma}{\nu}\right) t}. \tag{4}$$

In this equation, the Lamb constant α_{L} is equal to 1.25643, ν is the kinematic viscosity, and Squire's parameter a_1 is 0.1 according to Nguyen et al. [12]. The use of growing vortex cores helps the current aerodynamic model avoid the singularity problem due to the wing–wake interaction [12, 24].

The aerodynamic model based on the UVLM has been validated in our previous work [12, 13] for the aerodynamics of hawkmoths at various flight speeds. In this study, we apply this model for a hawkmoth model flying at a speed of 1 m/s in an asymmetric flight condition.

2.3 Multibody Dynamics Code and Simulation Framework

Insects are multibody dynamics systems that include 6 DOFs of the body motion and 3 DOFs related to the rotations of each wing relative to the body. Zhang and Sun [25] presented the multibody dynamic equations of insect flight in their work with the consideration of periodic aerodynamic and inertial loads due to the flapping motions of the wings. In this study, these equations are solved numerically by the multibody dynamics code of *MSC. Adams* software. The dynamics of our insect model could be presented by the set of differential equations as follows:

$$\mathbf{Q}\ddot{\mathbf{q}} + \boldsymbol{\eta}_{\mathrm{q}}^{\mathrm{T}} \boldsymbol{\lambda} - \mathbf{P}^{\mathrm{T}} \mathbf{G}(\mathbf{q}, \dot{\mathbf{q}}) = 0, \tag{5}$$

$$\boldsymbol{\eta}(\mathbf{q}, t) = 0, \tag{6}$$

where $\mathbf{Q}$ is the mass matrix of the present dynamic system; $\mathbf{q}$ denotes the set of coordinates representing displacements; $\boldsymbol{\eta}$ is the set of applied motion constraints that are expressed in Eq. (6); $\boldsymbol{\lambda}$ represents the Lagrange multipliers; $\mathbf{G}$ denotes the set of applied forces and gyroscopic terms of the inertia forces; $\mathbf{P}^{\mathrm{T}}$ is the matrix used to project the applied forces in the $\mathbf{q}$ direction.

Our simulation framework is developed in the environment of *MSC. Adams* utilizing the multibody dynamics solver that is coupled with the aerodynamic model presented in Sect. 2.2. The coupling procedure is illustrated in Fig. 3. The positions of the body and the wings are input to the aerodynamic model, while the aerodynamic loads computed by the aerodynamic model are exported to the multibody dynamics solver. The framework uses the GSTIFF integrator [26] to solve the differential Eqs. (5) and (6) with the prediction and correction phases. More details of the simulation framework can be found in references [14, 27]. The validity of this type of simulation framework with respect to the multibody dynamics of FWMAVs has been confirmed in many studies such as those by Nguyen et al. [13], Kim et al. [27], Pfeiffer et al. [28], and Lee et al. [29].

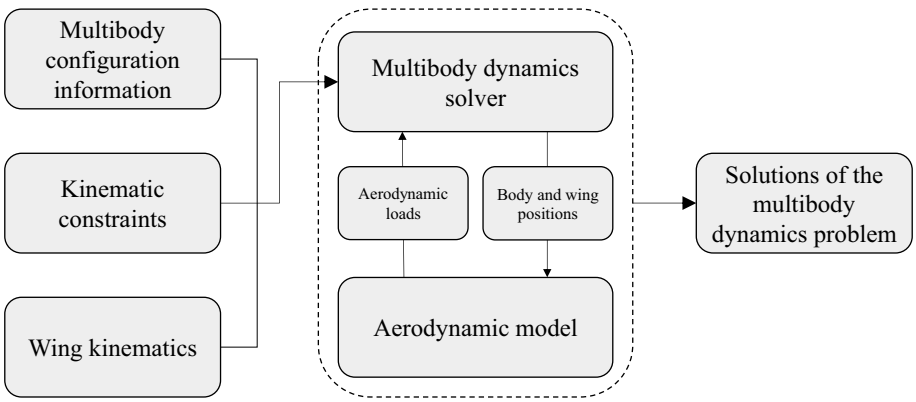

Fig. 3 Flowchart of the multibody dynamics simulation framework

2.4 Trim Search Algorithm

The trim search algorithm used in this paper to find the equilibrium flight state is similar to those utilized in studies by Nguyen et al. [13] and Kim et al. [14]. However, in the previous works, due to the symmetric flight condition, only the longitudinal motion variables were considered to search the trim states. In this study, the two wings are assumed asymmetric; thus, the whole 6 DOFs of the body motion must be involved. Corresponding to these 6 DOFs, six parameters related to the wing motion should be adjusted to balance the insect model. According to Kim and Han [30], the most effective control parameters corresponding to the 6 DOFs are the symmetric changes in the values of the peak-to-peak stroke amplitude ϕ_{amp}, mean sweep angle ϕ_0 and mean rotation angle α_0; and the asymmetric changes in the values of ϕ_{amp}, mean elevation angle θ_0 and mean rotation angle α_0. The symmetric changes are associated with identical adjustments of wing kinematics made on the left and right wings, whereas the asymmetric changes are related to adjustments that are equal in magnitude but opposite in sign. A clearer expression to explain this concept is given in Eq. (7) as follows:

$$\begin{aligned} X^{r} &= X_{ref} + \Delta X^{s} + \Delta X^{as}, \\ X^{l} &= X_{ref} + \Delta X^{s} - \Delta X^{as}. \end{aligned} \tag{7}$$

Here, X can be ϕ_{amp}, ϕ_0, θ_0 and α_0; X_{ref} is the reference value, which is determined from the measurement data of a living hawkmoth [16]; the superscripts r and l represent the right and left wing; while the superscripts s and as denote the symmetric and asymmetric changes, respectively. According to Willmott [16], the reference values of ϕ_{amp}, ϕ_0, θ_0 and α_0 are respectively 105.7°, −13.9°, −3.0° and 96.6°. It is noted that to tune the mean value of an angle, the coefficient a_0 in Eq. (1) is changed, whereas in the case of ϕ_{amp}, a_1 is adjusted because the function $\phi(t)$ has an almost cosine form.

In this work, we will replace the symmetric change in the peak-to-peak stroke amplitude ϕ_{amp} by the symmetric change in the flapping frequency f to avoid the possible problem of wing-wing intersection. In fact, Δf^{s} and $\Delta\phi^{s}_{amp}$ have the same control effectiveness effect, since they both primarily affect the average lift force [13, 30]. The reference value of f is 25.4 Hz.

The flowchart of the trim search algorithm is shown in Fig. 4. First, external forces and moments are applied to the insect model to offset the average inertial forces and moments at the body center after one wingbeat stroke cycle. After that, the initial velocities are modified to balance the model. Once the model has been balanced, the wing kinematics is adjusted to generate excessive forces and moments

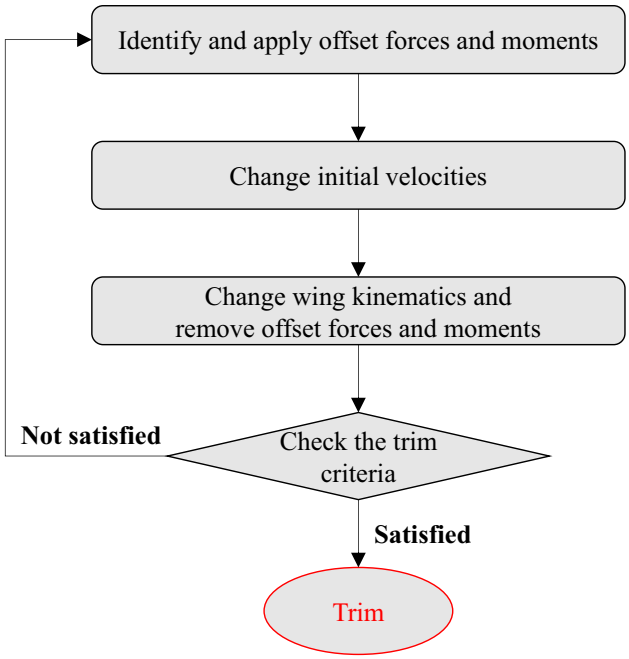

Fig. 4 Flowchart of the trim search algorithm

to replace the applied offset forces. Here, we adjust the wing kinematics using the control effectiveness matrix **B**:

$$\mathbf{B} = \begin{bmatrix} \frac{\partial \bar{F}_{x_G}}{\partial(\Delta f^{s})} & \frac{\partial \bar{F}_{x_G}}{\partial(\Delta \phi_0^{s})} & \frac{\partial \bar{F}_{x_G}}{\partial(\Delta \alpha_0^{s})} & \frac{\partial \bar{F}_{x_G}}{\partial(\Delta \phi_{amp}^{as})} & \frac{\partial \bar{F}_{x_G}}{\partial(\Delta \theta_0^{as})} & \frac{\partial \bar{F}_{x_G}}{\partial(\Delta \alpha_0^{as})} \\ \frac{\partial \bar{F}_{y_G}}{\partial(\Delta f^{s})} & \frac{\partial \bar{F}_{y_G}}{\partial(\Delta \phi_0^{s})} & \frac{\partial \bar{F}_{y_G}}{\partial(\Delta \alpha_0^{s})} & \frac{\partial \bar{F}_{y_G}}{\partial(\Delta \phi_{amp}^{as})} & \frac{\partial \bar{F}_{y_G}}{\partial(\Delta \theta_0^{as})} & \frac{\partial \bar{F}_{y_G}}{\partial(\Delta \alpha_0^{as})} \\ \frac{\partial \bar{F}_{z_G}}{\partial(\Delta f^{s})} & \frac{\partial \bar{F}_{z_G}}{\partial(\Delta \phi_0^{s})} & \frac{\partial \bar{F}_{z_G}}{\partial(\Delta \alpha_0^{s})} & \frac{\partial \bar{F}_{z_G}}{\partial(\Delta \phi_{amp}^{as})} & \frac{\partial \bar{F}_{z_G}}{\partial(\Delta \theta_0^{as})} & \frac{\partial \bar{F}_{z_G}}{\partial(\Delta \alpha_0^{as})} \\ \frac{\partial \bar{M}_{x_G}}{\partial(\Delta f^{s})} & \frac{\partial \bar{M}_{x_G}}{\partial(\Delta \phi_0^{s})} & \frac{\partial \bar{M}_{x_G}}{\partial(\Delta \alpha_0^{s})} & \frac{\partial \bar{M}_{x_G}}{\partial(\Delta \phi_{amp}^{as})} & \frac{\partial \bar{M}_{x_G}}{\partial(\Delta \theta_0^{as})} & \frac{\partial \bar{M}_{x_G}}{\partial(\Delta \alpha_0^{as})} \\ \frac{\partial \bar{M}_{y_G}}{\partial(\Delta f^{s})} & \frac{\partial \bar{M}_{y_G}}{\partial(\Delta \phi_0^{s})} & \frac{\partial \bar{M}_{y_G}}{\partial(\Delta \alpha_0^{s})} & \frac{\partial \bar{M}_{y_G}}{\partial(\Delta \phi_{amp}^{as})} & \frac{\partial \bar{M}_{y_G}}{\partial(\Delta \theta_0^{as})} & \frac{\partial \bar{M}_{y_G}}{\partial(\Delta \alpha_0^{as})} \\ \frac{\partial \bar{M}_{z_G}}{\partial(\Delta f^{s})} & \frac{\partial \bar{M}_{z_G}}{\partial(\Delta \phi_0^{s})} & \frac{\partial \bar{M}_{z_G}}{\partial(\Delta \alpha_0^{s})} & \frac{\partial \bar{M}_{z_G}}{\partial(\Delta \phi_{amp}^{as})} & \frac{\partial \bar{M}_{z_G}}{\partial(\Delta \theta_0^{as})} & \frac{\partial \bar{M}_{z_G}}{\partial(\Delta \alpha_0^{as})} \end{bmatrix}. \tag{8}$$

In this matrix, the aerodynamic forces and moments F and M are calculated in the ground-fixed coordinate system. The over bar represents the cycle average value. The wing kinematics are modified through the six aforementioned parameters, including Δf^{s}, $\Delta\phi_0^{s}$, $\Delta\alpha_0^{s}$, $\Delta\phi_{amp}^{as}$, $\Delta\theta_0^{as}$ and $\Delta\alpha_0^{as}$. The wing kinematics of the $(k+1)^{th}$ iteration can be determined by

$$\begin{bmatrix} \Delta f^{s} \\ \Delta \phi_0^{s} \\ \Delta \alpha_0^{s} \\ \Delta \phi_{amp}^{as} \\ \Delta \theta_0^{as} \\ \Delta \alpha_0^{as} \end{bmatrix}_{k+1} = \begin{bmatrix} \Delta f^{s} \\ \Delta \phi_0^{s} \\ \Delta \alpha_0^{s} \\ \Delta \phi_{amp}^{as} \\ \Delta \theta_0^{as} \\ \Delta \alpha_0^{as} \end{bmatrix}_{k} + \mathbf{B}^{-1} \begin{bmatrix} \Delta F_{x_G} \\ \Delta F_{y_G} \\ \Delta F_{z_G} \\ \Delta M_{x_G} \\ \Delta M_{y_G} \\ \Delta M_{z_G} \end{bmatrix}_{k}. \quad (9)$$

In this equation, ΔF and ΔM are the offset forces and moments. The trim criteria are satisfied if the mean velocity of the insect model is close to the reference velocity, and the offset forces and moments are small.

The trim search program uses the reference wing kinematics as the initial guess of the solution. The initial values of the six parameters in Eq. (9) are, therefore, set to be zero. The trimmed flight state must guarantee that the mean stroke plane angle β and the mean body angle χ are equal to their reference values. According to Willmott [16], β and χ are 24.4° and 31.3°, respectively, for the living hawkmoth.

3 Results and Discussion

3.1 Trim Conditions

The present insect model flies forward at a slow speed of 1 m/s with the right wing 10% heavier than the left wing. The advance ratio is about 0.4 based on the mean wing velocity. Herein, the mean wing velocity is defined as $2f\phi_{amp}r_2$, in which r_2 is the radius of the second moment of the wing area. Equilibrium flight is obtained by applying the trim search algorithm (Sect. 2.4) along with the multibody dynamics simulation framework (Sect. 2.3). The trim wing kinematics is represented by the variations of the position angles ϕ, θ and α of the left and right wings, which are shown in Fig. 5. Here, the solid lines are corresponding to the wing kinematics of the right wing, while the dashed lines show that of the left wing. It is seen that the most obvious difference between the motions of the two wings is in the peak-to-peak stroke amplitude ϕ_{amp}. The peak-to-peak stroke amplitude of the right wing (heavier wing) is about 10° larger than that of the left wing. The wing mass asymmetry results in a negative moment about the x_G axis of the ground-fixed coordinate system. To compensate for this moment, the right wing has to generate more lift than the left one. Kim and Han found that ϕ_{amp} is the only effective control variable for the lift force [30]. Therefore, the insect has to move the right wing with larger stroke amplitude to regain the equilibrium state, while the differences in the other variables between the left and right wings are small.

The flapping frequency f in the trim condition is 27.8 Hz, which is slightly higher than the reference value. The large flapping frequency may be attributed to the use of the rigid wings. At the same value of f, due to wing deformation, a flexible wing can produce more lift than a rigid one. Therefore, compared to an actual hawkmoth wing, the present insect model needs to move its wings slightly faster to generate enough lift.

Figure 6 illustrates the wake visualization at 1.8 wingbeat stroke cycle and the downward velocity of the flow at a vertical plane right behind the wings. It is seen that the right wing generates a stronger downward flow than the left wing; therefore, wake sheets behind the right wing move downward faster. The stronger downward flow is related to

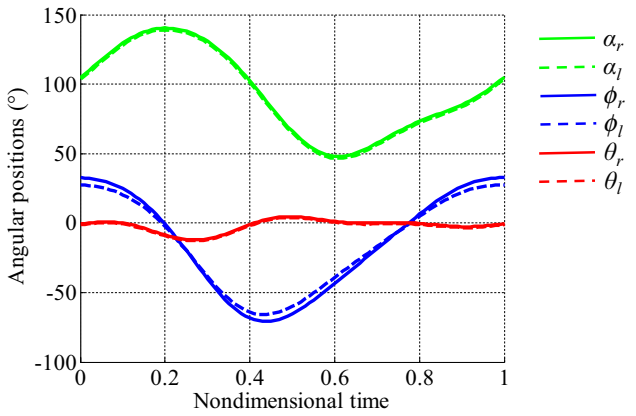

Fig. 5 Wing kinematics in the trim flight

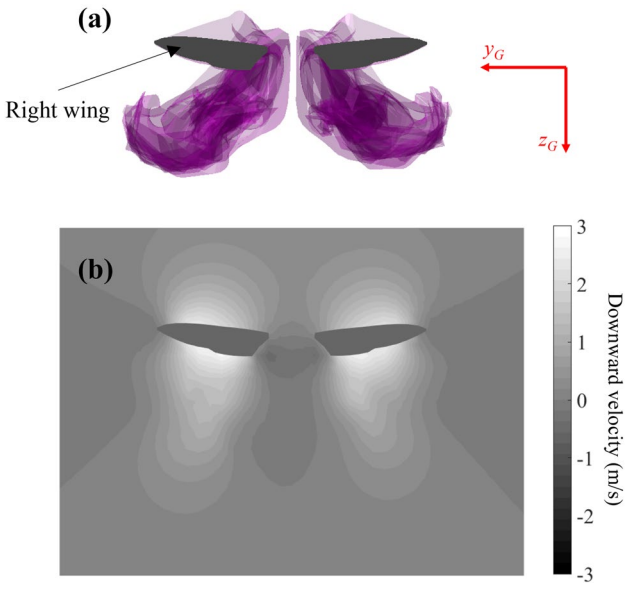

Fig. 6 Wake visualization (**a**) and downward flow velocity at a vertical plane right behind the wings (**b**) after 1.8 wingbeat stroke cycles

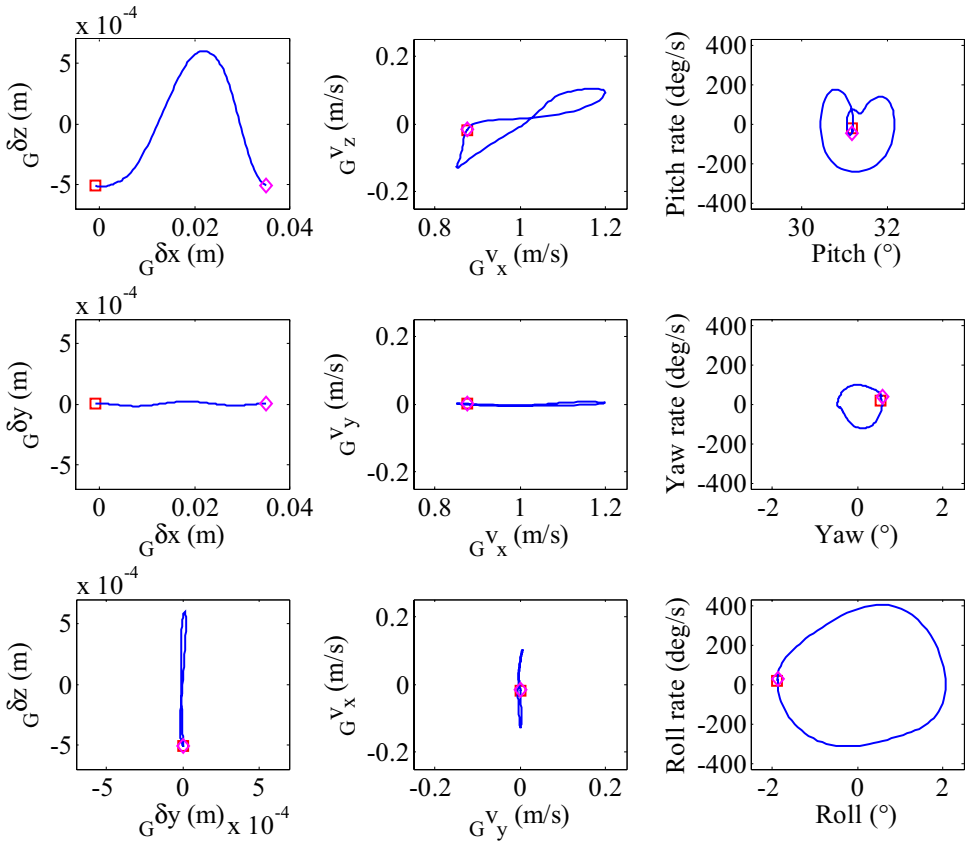

Fig. 7 Flight trajectory and phase portraits of trim flight in one wingbeat stroke cycle

the higher lift force on the right wing according to the law of conservation of momentum.

The closed-loop phase portraits in Fig. 7 indicate that the trim criteria in this study are satisfied. Here, the subscript G refers to the ground-fixed coordinate system. The figure reveals that the lateral translational displacement and its velocity are small. The peak-to-peak amplitude of the lateral displacement ${}_{G}\delta y$ is only 0.037 mm, compared to 1.12 mm of the vertical displacement ${}_{G}\delta z$. Similarly, the peak-to-peak variation amplitude of the lateral velocity ${}_{G}v_y$ is only 0.011 m/s, which is much lower than 0.35 and 0.23 m/s of the horizontal and vertical velocities ${}_{G}v_x$ and ${}_{G}v_z$, respectively. The roll motion is more considerable than the yaw and pitch motions. The peak-to-peak amplitudes of the roll angle and roll rate are, respectively, 3.96° and 717.93 deg/s, compared to 1.73° and 417.73 deg/s of the pitch motion, and 1.05° and 221.17 deg/s of the yaw motion. The large oscillation about the roll direction can be explained by the small value of I_{x_b} (moment of inertia with respect to the center of mass about the x_b axis), which is estimated to be 1.10×10^{-7} kg m^2, compared to 2.84×10^{-7} kg m^2 of I_{y_b} and 3.48×10^{-7} kg m^2 of I_{z_b}.

3.2 Power Requirements

As mentioned earlier, each wing is connected to the body by a 3-DOF revolute joint corresponding to the set of three Euler angles ϕ, θ, and α. Therefore, the required mechanical power P of each wing can be calculated as the sum of P_ϕ, P_θ and P_α that are needed to rotate the wing about its sweeping, elevating, and rotating axes, respectively. In this work, we investigate two possibilities of the power storage mechanism of insect flight [31]. For the first possibility, when the wing does negative work, the energy is stored by elastic elements, and during the period of positive work, this energy is released. Hence, the power components P_ϕ, P_θ and P_α can be expressed as

$$P_j = \tau_j \frac{dj}{dt}, \quad (j = \phi, \theta, \alpha), \tag{10}$$

where τ_j is the torque about the j axis computed at the revolute joint. The second possibility is that the negative power is entirely dissipated and the elastic mechanism of power storage is not allowed in our system. In this case, the power components are calculated as follows:

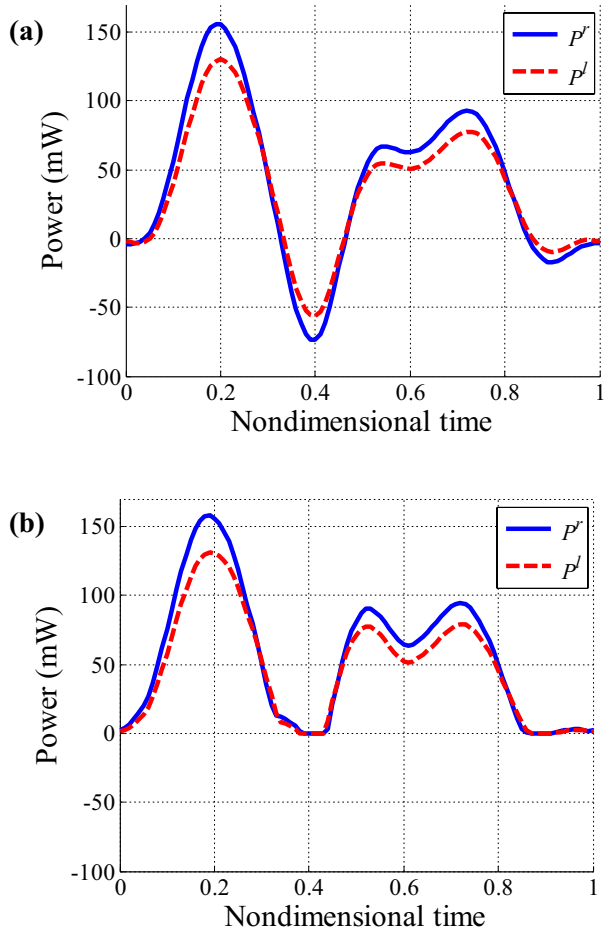

Fig. 8 The variations of the total power required by the right wing P^{r} and that by the left wing P^{l} in one wingbeat stroke cycle when the negative energy is stored by elastic elements (**a**), and without the elastic storage mechanism (**b**)

$$\begin{aligned} P_j &= \tau_j \frac{dj}{dt} \quad \text{if } \tau_j \frac{dj}{dt} > 0, \\ P_j &= 0 \qquad \text{if } \tau_j \frac{dj}{dt} \le 0, \quad j = \phi,\ \theta,\ \alpha. \end{aligned} \tag{11}$$

The torque τ_j in Eqs. (10) and (11) could be decomposed into the inertial component required to overcome the inertial force, and the aerodynamic component to overcome the aerodynamic force. These components are corresponding to the inertial power P^{i} and the aerodynamic power P^{a}, respectively. According to Willmott and Ellington [31], the magnitude of the inertial power P^{i} can be roughly estimated to be proportional to $I_{\mathrm{wg}} \times \left(\phi_{\mathrm{amp}}\right)_3^2$, and that of the aerodynamic P^{a} is proportional to $\left(\phi_{\mathrm{amp}}\right)^3$. Here, I_{wg} is the moment of inertia of the wing. The right wing has the larger peak-to-peak stroke amplitude ϕ_{amp} and the greater inertia moment; thus, it is expected to require more power than the left wing. It should be noted that when the elastic storage mechanism

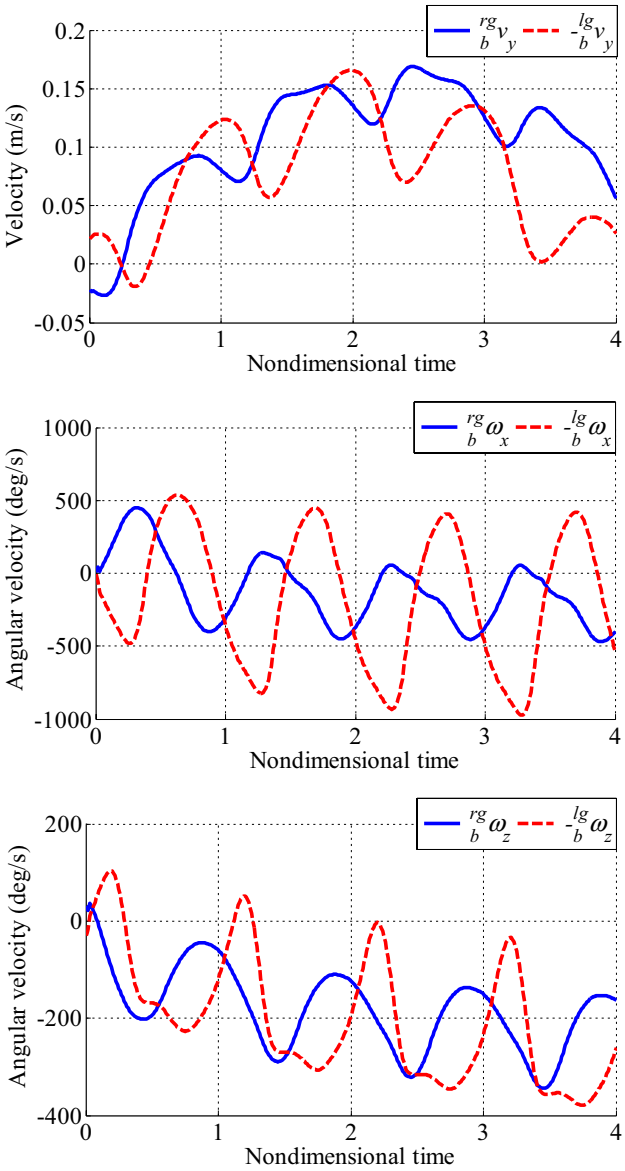

Fig. 9 Lateral dynamic responses of the insect model to the rightward and leftward gust disturbances within the first four wingbeat stroke cycles

is used, the positive and negative amounts of energy due to the inertial torque almost cancel each other out. Thus, the contribution of work done by the inertial torque to the overall result in one wingbeat stroke cycle is small. The time histories of the total power required by the right wing P^{r} and that by the left wing P^{l} corresponding to the first and second possibilities are shown in Fig. 8a, b. Based on the numerical data, the total mechanical power demands by the right and left wings are 40.6 mW and 35.6 mW for the case of elastic storage mechanism, and 56.09 mW and 47.82 mW for the case of no elastic storage mechanism, respectively. These results indicate that the heavier wing consumes 14%

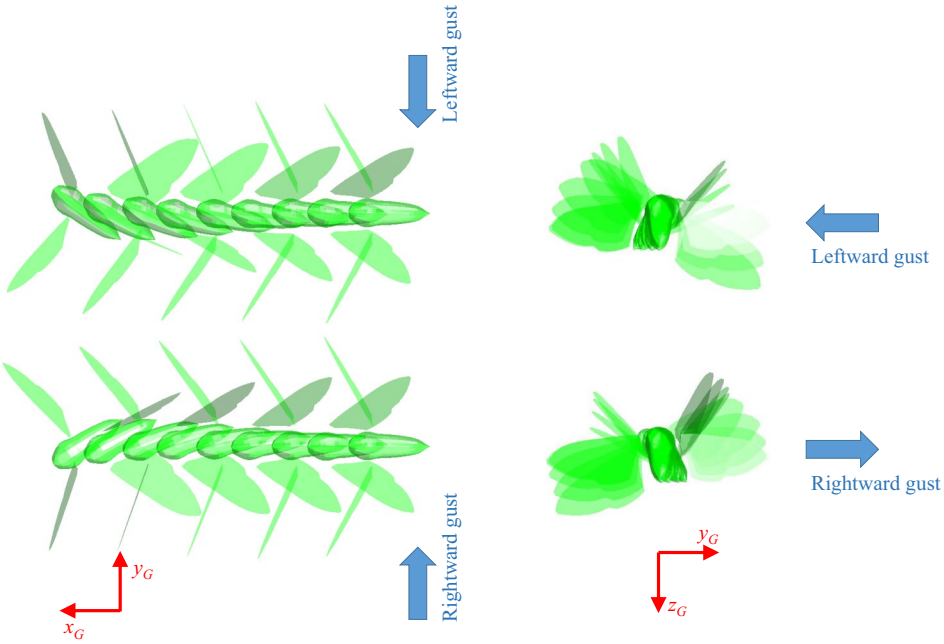

Fig. 10 Flight trajectories of the insect model due to the rightward and leftward gust disturbances in the first four wingbeat stroke cycles

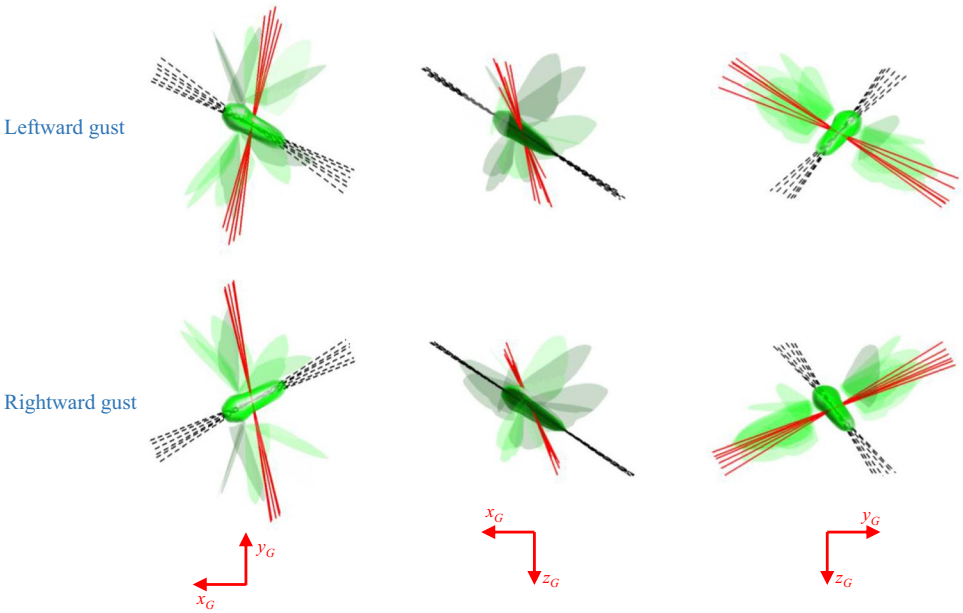

Fig. 11 Orientation of the insect body in the cases of rightward and leftward gust disturbances in the fourth wingbeat stroke cycle

and 17% more energy than the lighter wing corresponding to the cases with and without elastic storage mechanism, respectively.

3.3 Dynamic Responses to Lateral Gusts

In order to gain more insight into the asymmetric properties of the present insect model, two lateral constant gust disturbances with the same magnitude of 20% of the mean wing velocity and opposite directions (rightward vs. leftward) are applied. The dynamic responses of the insect model to the rightward and leftward gust disturbances in the first four wingbeat stroke cycles are exhibited in Fig. 9. Here, due to the inconsiderable effect of lateral disturbances on longitudinal dynamics [27], we consider only lateral dynamic variables, including ${}_{\mathrm{b}}v_y$ (translational velocity on the y_{b} axis), and ${}_{\mathrm{b}}\omega_x$ and ${}_{\mathrm{b}}\omega_z$ (angular velocities about the x_{b} and z_{b} axes). The subscript b is used to indicate that these variables are measured in the body-fixed coordinate system. In Fig. 9, the variables corresponding to the leftward gust disturbance are displayed with an opposite sign. In general, the responses to the two types of gust disturbances show similar overall

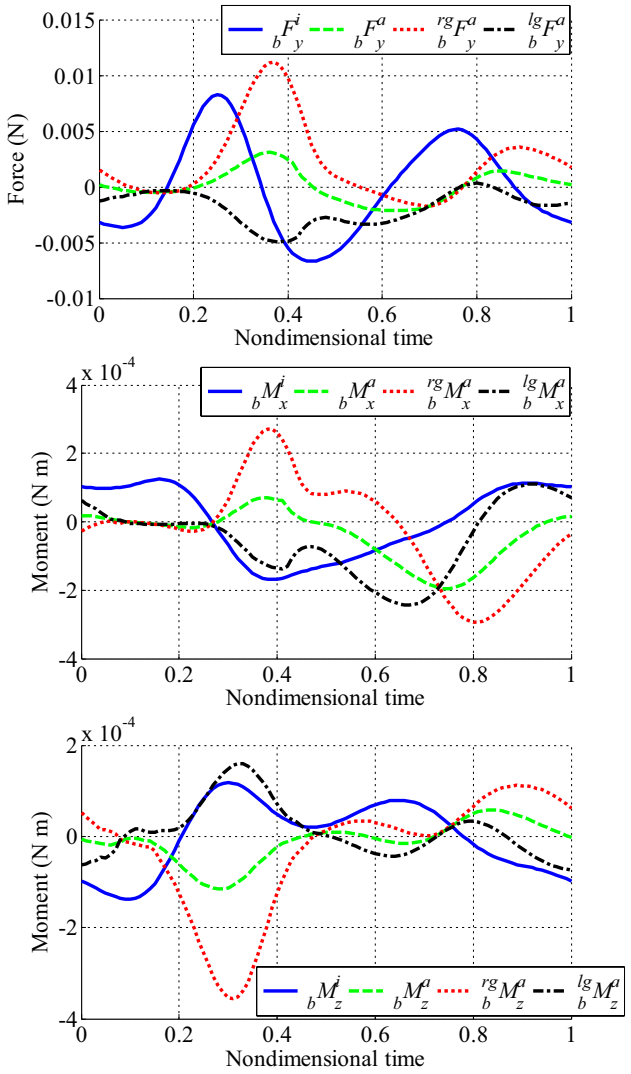

Fig. 12 Lateral components of the inertial and aerodynamic forces F^{i} and F^{a}, and moments M^{i} and M^{a} in three cases: rightward gust, leftward gust and without gust

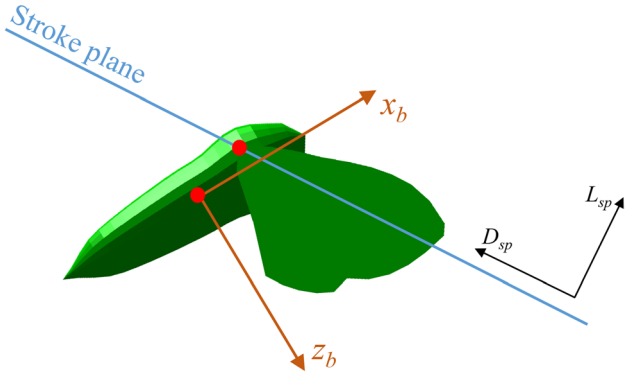

Fig. 13 Lift and drag acting on the wing in the stroke plane frame L_{sp} and D_{sp}

trends as indicated in Figs. 9 and 10; however, when the leftward gust is applied, the angular velocities vary with the larger amplitudes; hence, the insect model tends to oscillate more strongly. The differences in the phase are also observed in Fig. 9. To illustrate this asymmetry in dynamic response, the variation of the body orientation in the fourth wingbeat stroke cycle is displayed in Fig. 11. In this figure, the translational displacements are not shown, and the orientation represented by the dashed line (x_{b} axis) and solid line (y_{b} axis) after each 20% of the wingbeat stroke cycle is exhibited. Figure 11 shows the larger oscillation of the body orientation in the case of the leftward gust than that corresponding to the rightward gust. The peak-to-peak amplitudes of roll and yaw angles within the fourth stroke cycle in the case of the leftward gust are approximately 15° and 11°, respectively; while those in the case of the rightward gust are 11° and 9°.

The responses to the two types of gust are similar in overall trend; the significant difference is observed only within each wingbeat stroke cycle (Figs. 9 and 10). Therefore, the cycle-average approach, which ignores the variations of the dynamic variables within each wingbeat cycle as shown in many previous studies [13, 14, 32, 33], cannot explain this difference. In an effort to explain the asymmetry of the dynamic responses due to the rightward and leftward gust disturbances, the lateral components of inertial and aerodynamic forces and moments are computed and exhibited in Fig. 12. In this figure, the aerodynamic forces and moments corresponding to the three cases of the rightward gust, the leftward gust and without gust are presented. It is noted that the moments discussed here are calculated with respect to the center of mass of the insect model. The first plot shows that the rightward gust and leftward gust provide positive and negative additional forces on the y_{b} axis, respectively. The peaks of these additional forces appear at the end of the upstroke (about 0.4 of the wingbeat stroke cycle) because at this moment, the wings have the largest lateral cross sections due to the highest value of the sweep angle ϕ (Fig. 5). To explain the trends of the moments ${}_{\mathrm{b}}M_x$ and ${}_{\mathrm{b}}M_z$ about the x_{b} and z_{b} axes, it is necessary to have a look at the relative position of the stroke plane to the body. An angle between the body axis and the stroke plane is estimated to be about 60° for the hawkmoth *Manduca sexta* [34] as illustrated in Fig. 13. With this angle, the asymmetry in the lift force given in the stroke plane frame L_{sp} between the two wings will primarily cause ${}_{\mathrm{b}}M_z$ (moment about the z_{b} axis). On the other hand, the moment ${}_{\mathrm{b}}M_x$ is mainly caused by the asymmetry in the drag force D_{sp}. Based on the knowledge of the changing-relative-velocity effect, which was mentioned by Sun in Ref. [35] to clarify the difference in relative velocity of the left and right wings

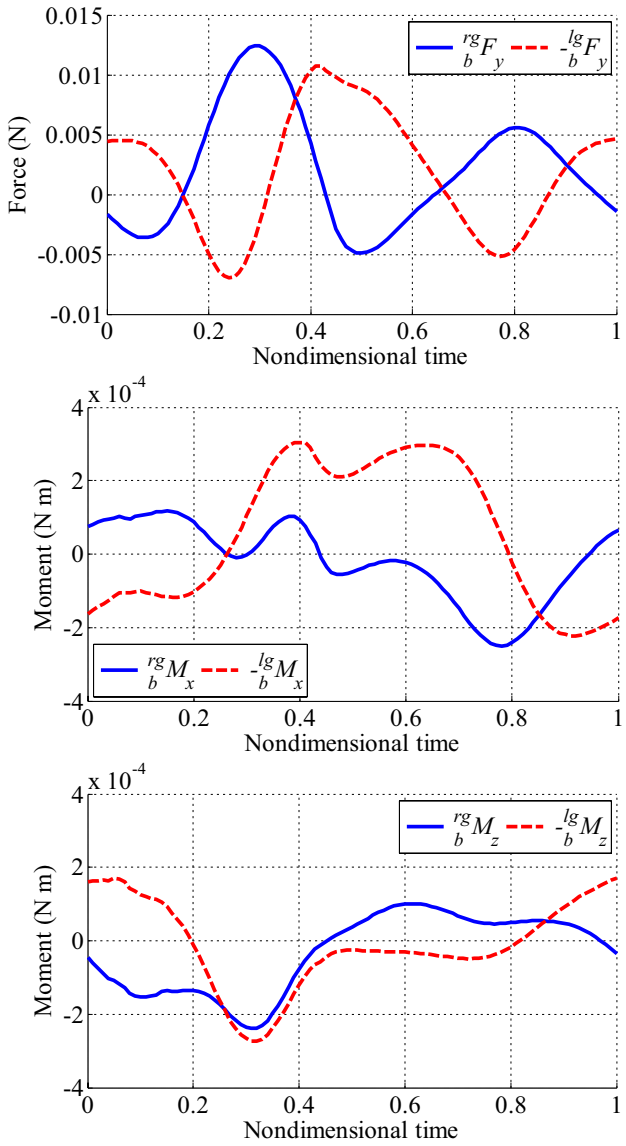

Fig. 14 Lateral components of total force F and moment M acting on the insect model due to rightward and leftward gust disturbances

while experiencing a lateral wind, we can easily explain the trends of the moments ${}_{\mathrm{b}}M_x$ and ${}_{\mathrm{b}}M_z$ shown in Fig. 12. According to this effect, in the case of the rightward gust, the difference in D_{sp} between the right and left wings due to the gust velocity is negative when the sweep angle ϕ is negative, and that negative difference in D_{sp} will cause a positive additional moment to ${}_{\mathrm{b}}M_x$. From the variations of the position angles shown in Fig. 5, we can deduce that the rightward gust will increase the moment ${}_{\mathrm{b}}M_x$ during the period between 0.2 and 0.8 of the wingbeat stroke cycle (Fig. 12). The difference in L_{sp} between the right and left wings is positive when the sweep angle ϕ is negative and the rotation angle α is less than 90°, or the sweep angle ϕ is positive and the rotation angle α is more than 90°. The positive value of the difference in L_{sp} is corresponding a negative additional value of ${}_{\mathrm{b}}M_z$. From Fig. 5, it can follow that the rightward gust enhances ${}_{\mathrm{b}}M_z$ during the periods from 0.2 to 0.45 and from 0.8 to 1.0 of the wingbeat stroke cycle as shown in Fig. 12. The trends of the moments ${}_{\mathrm{b}}M_x$ and ${}_{\mathrm{b}}M_z$ due to the leftward gust disturbance may be explained in the same way.

Now, we can see that the inertial moment ${}_{\mathrm{b}}M_x^{\mathrm{i}}$ about the x_{b} axis is in phase with the variation of the aerodynamic moment ${}_{\mathrm{b}}^{\mathrm{lg}}M_x^{\mathrm{a}}$ due to the leftward gust, and almost 180° out of phase with the rightward-gust aerodynamic moment ${}_{\mathrm{b}}^{\mathrm{rg}}M_x^{\mathrm{a}}$. A similar trend is observed for the inertial and aerodynamic moments about the z_{b} axis. Due to these differences in the phases, the total moments acting on the insect model (sum of inertial and aerodynamic moments) in the case of the leftward gust will have the greater variation amplitudes (Fig. 14). These greater amplitudes will lead to the stronger oscillations in Fig. 9. Figure 14 also shows the phase differences between the total forces and moments due to the rightward and leftward gust disturbances. These phase differences in terms of forces and moments account for those in terms of responses as shown in Fig. 9.

4 Conclusions

In this paper, we discuss the effect of wing mass asymmetry on the low-speed flight characteristics, such as the trim conditions, the power requirements and the dynamic responses of a hawkmoth model. The results show that the heavier wing has to have a larger stroke amplitude to generate more lift in order to compensate for the asymmetry in the wing mass. Moreover, the downward flow and the power requirement of the heavier wing are greater. In the present paper, the right wing is assumed 10% heavier than the left wing, and in the trim conditions, this wing is estimated to have a 10° larger peak-to-peak stroke amplitude and consumes approximately 14% and 17% more power than the left wing corresponding to the cases with and without the elastic storage mechanism, respectively. When the phase portraits of trim flight are studied, it is observed that the roll oscillation is significant because of the small value of moment of inertia about the body axis $I_{x_{\mathrm{b}}}$. The study also presents the asymmetry in the dynamic characteristics of the insect model. For the model with the heavier right wing, its passive dynamic responses to the leftward gust disturbance show the more considerable oscillation amplitudes than those corresponding to the rightward gust disturbance. Furthermore, differences in the phase between these responses are observed. The asymmetry in the dynamic responses due to the rightward and leftward gust disturbances is attributed to the asymmetry in total forces and moments that are the combinations of the inertial and aerodynamic forces and

moments. Specifically, when the leftward gust is applied, the inertial and aerodynamic moments are almost in phase; however, they become 180° out of phase in the case of the rightward gust.

It is obvious that with 10% of the difference in wing mass, the low-speed flight performance could be affected significantly. In fact, with another amount of wing mass asymmetry or at another flight speed, the result will probably be quantitatively different. However, the physical bases and the overall trends of the results should be similar to those obtained in the present study. Some conclusions drawn in this paper could be found useful while designing insect-like FWMAVs as well as developing fight control algorithms. In reality, wing mass asymmetry may go with differences in wing shape and area, and the effects of these factors should be investigated in future work.

Acknowledgements This research is funded by Vietnam National Foundation for Science and Technology Development (NAFOSTED) under Grant Number 107.01-2018.05.

References

1. Phan HV, Kang T, Park HC (2017) Design and stable flight of a 21 g insect-like tailless flapping wing micro air vehicle with angular rates feedback control. Bioinspir Biomim 12:036006. https://doi.org/10.1088/1748-3190/aa65db
2. Keennon M, Klingebiel K (2012) Development of the nano hummingbird: a tailless flapping wing micro air vehicle. AIAA aerospace sciences meeting, Reston, Virginia, US. https://doi.org/10.2514/6.2012-588
3. Ma KY, Chirarattananon P, Fuller SB, Wood RJ (2013) Controlled flight of a biologically inspired, insect-scale robot. Science 340:603–607. https://doi.org/10.1126/science.1231806
4. Karásek M, Hua A, Nan Y, Lalami M, Preumont A (2014) Pitch and roll control mechanism for a hovering flapping wing MAV. Int J Micro Air Veh 6:253–264. https://doi.org/10.1260/1756-8293.6.4.253
5. Chan WL, Nguyen QV, Debiasi M (2016) Tailless control of a double clap-and-fling flapping wing MAV. In: International micro air vehicle competition and conference, Beijing, China
6. Muijres FT, Elzinga MJ, Melis JM, Dickinson MH (2014) Flies evade looming targets by executing rapid visually directed banked turns. Science 344:172–177. https://doi.org/10.1126/science.1248955
7. Meng XG, Sun M (2016) Wing and body kinematics of forward flight in drone-flies. Bioinspir Biomim 11:056002. https://doi.org/10.1088/1748-3190/11/5/056002
8. O'Hara RP, Palazotto AN (2012) The morphological characterization of the forewing of the *Manduca sexta* species for the application of biomimetic flapping wing micro air vehicles. Bioinspir Biomim 7:046011. https://doi.org/10.1088/1748-3182/7/4/046011
9. Fernandez MJ, Springthorpe D, Hedrick TL (2012) Neuromuscular and biomechanical compensation for wing asymmetry in insect hovering flight. J Exp Biol 215:3631–3638. https://doi.org/10.1242/jeb.073627
10. Muijres FT, Iwasaki NA, Elzinga MJ, Melis JM, Dickinson MH (2017) Flies compensate for unilateral wing damage through modular adjustments of wing and body kinematics. Interface Focus 7:20160103. https://doi.org/10.1098/rsfs.2016.0103
11. Kassner Z, Dafni E, Ribak G (2016) Kinematic compensation for wing loss in flying damselflies. J Insect Physiol 85:1–9. https://doi.org/10.1016/j.jinsphys.2015.11.009
12. Nguyen AT, Kim J-K, Han J-S, Han J-H (2016) Extended unsteady vortex-lattice method for insect flapping wings. J Aircr 53:1709–1718. https://doi.org/10.2514/1.C033456
13. Nguyen AT, Han J-S, Han J-H (2017) Effect of body aerodynamics on the dynamic flight stability of the hawkmoth *Manduca sexta*. Bioinspir Biomim 12:016007. https://doi.org/10.1088/1748-3190/12/1/016007
14. Kim JK, Han JS, Lee JS, Han JH (2015) Hovering and forward flight of the hawkmoth *Manduca sexta*: trim search and 6-DOF dynamic stability characterization. Bioinspir Biomim 10:056012. https://doi.org/10.1088/1748-3190/10/5/056012
15. Ellington CP (1984) The aerodynamics of hovering insect flight. II. Morphological parameters. Philos Trans R Soc Lond B Biol Sci 305:17–40. https://doi.org/10.1098/rstb.1984.0050
16. Willmott AP (1995) The mechanics of hawkmoth flight. Dissertation, University of Cambridge
17. Senda K, Obara T, Kitamura M, Yokoyama N, Hirai N, Iima M (2012) Effects of structural flexibility of wings in flapping flight of butterfly. Bioinspir Biomim 7:025002. https://doi.org/10.1088/1748-3182/7/2/025002
18. Senda K, Obara T, Kitamura M, Nishikata T, Hirai N, Iima M, Yokoyama N (2012) Modeling and emergence of flapping flight of butterfly based on experimental measurements. Robot Auton Syst 60:670–678. https://doi.org/10.1016/j.robot.2011.12.007
19. Roccia BA, Preidikman S, Massa JC, Mook DT (2013) Modified unsteady vortex-lattice method to study flapping wings in hover flight. AIAA J 51:2628–2642. https://doi.org/10.2514/1.J052262
20. Nguyen AT, Han J-H, Nguyen AT (2017) Application of artificial neural networks to predict dynamic responses of wing structures due to atmospheric turbulence. Int J Aeronaut Space Sci 18:474–484. https://doi.org/10.5139/IJASS.2017.18.3.474
21. Ellington CP, van den Berg C, Willmott AP, Thomas ALR (1996) Leading-edge vortices in insect flight. Nature 384:626–630. https://doi.org/10.1038/384626a0
22. Polhamus EC (1971) Predictions of vortex-lift characteristics by a leading-edge suction analogy. J Aircr 8:193–199. https://doi.org/10.2514/3.44254
23. Gandhi F, Tauszig L (2000) A critical evaluation of various approaches for the numerical detection of helicopter blade-vortex interactions. J Am Helicopter Soc 45:179–190. https://doi.org/10.4050/JAHS.45.179
24. Zhang YL, Sun M (2010) Dynamic flight stability of hovering model insects: theory versus simulation using equations of motion coupled with Navier–Stokes equations. Acta Mech Sin 26:509–520. https://doi.org/10.1007/s10409-010-0360-5
25. Gear C (1971) Simultaneous numerical solution of differential-algebraic equations. IEEE Trans Circuit Theory 18:89–95. https://doi.org/10.1109/TCT.1971.1083221
26. Kim J-K, Han J-H (2014) A multibody approach for 6-DOF flight dynamics and stability analysis of the hawkmoth *Manduca sexta*. Bioinspir Biomim 9:016011. https://doi.org/10.1088/1748-3182/9/1/016011
27. Pfeiffer AT, Lee J-S, Han J-H, Baier H (2010) Ornithopter flight simulation based on flexible multi-body dynamics. J Bionic Eng 7:102–111. https://doi.org/10.1016/S1672-6529(09)60189-X
28. Lee JS, Kim JK, Han JH, Ellington CP (2012) Periodic tail motion linked to wing motion affects the longitudinal stability of

ornithopter flight. J Bionic Eng 9:18–28. https://doi.org/10.1016/S1672-6529(11)60093-0
29. Kim JK, Han JH (2013) Control effectiveness analysis of the hawkmoth *Manduca sexta*: a multibody dynamics approach. Int J Aeronaut Space Sci 14:152–161. https://doi.org/10.5139/ijass.2013.14.2.152
30. Casey TM (1981) A comparison of mechanical and energetic estimates of flight cost for hovering sphinx moths. J Exp Biol 91:117–129
31. Willmott AP, Ellington CP (1997) The mechanics of flight in the hawkmoth *Manduca sexta*. II. Aerodynamic consequences of kinematic and morphological variation. J Exp Biol 200:2723–2745
32. Taylor GK, Thomas ALR (2003) Dynamic flight stability in the desert locust *Schistocerca gregaria*. J Exp Biol 206:2803–2829. https://doi.org/10.1242/jeb.00501
33. Xu N, Sun M (2014) Lateral flight stability of two hovering model insects. J Bionic Eng 11:439–448. https://doi.org/10.1016/S1672-6529(14)60056-1
34. Willmott AP, Ellington CP (1997) The mechanics of flight in the hawkmoth *Manduca sexta*. I. Kinematics of hovering and forward flight. J Exp Biol 200:2705–2722
35. Sun M (2014) Insect flight dynamics: stability and control. Rev Mod Phys 86:615–646. https://doi.org/10.1103/RevModPhys.86.615